RESEARCH ARTICLE

Check for updates

Thiacalixarene-based {Co/Fe}$_{16}$ coordination clusters: bimetallic synergistic effect for an enhanced oxygen evolution reaction†

Xinxin Hang,[a,b] Xiaoju Wang,[a] Meilin Wang,[b] Mengwei Chen[b] and Yanfeng Bi (ID) *[b]

The integration of heterometallic units into coordination clusters used for the oxygen evolution reaction (OER) can enhance their electrocatalytic performance. Herein, we report the syntheses of a series of coordination clusters, namely **Co$_{16}$**, **{CoFe}$_{16}$-a**, **{CoFe}$_{16}$-b**, **{CoFe}$_{16}$-c** and **Fe$_{16}$**, assembled from different metal precursors (CoCl$_2$·6H$_2$O and/or FeCl$_3$·6H$_2$O), *p-tert*-butylsulfonylcalix[4]arene (H$_4$TC4A-SO$_2$), and 1,3-bis(2*H*-tetrazol-5-yl)benzene (BTTAB). These clusters feature box-like entities in which four M$_4$-(TC4A-SO$_2$) polynuclear secondary building units (PSBUs) in a square arrangement are bridged by eight BTTAB ligands. Among these PSBU-based coordination clusters, **{CoFe}$_{16}$-b** exhibits a better OER activity with an overpotential of 285.3 mV at a current density of 10 mA cm^{-2} and a Tafel slope of 72.8 mV dec^{-1} due to the synergistic effect between Co and Fe with an optimized molar ratio.

Introduction

The oxygen evolution reaction (OER) is an indispensable half-reaction for water splitting and has attracted great research interest.[1–4] It is well-known that iridium and ruthenium oxides are the most active electrocatalysts for the OER.[5,6] However, these electrocatalysts are extremely scarce and expensive which restricts their large-scale applications.[7,8] Thus, the search for cost-effective electrocatalysts with high OER activity is significant but exceedingly challenging.

Transition-metal-based coordination materials have aroused enormous attention for energy-related applications owing to their diversity in functional species of metal sites and organic ligands.[9–13] However, low conductivity and unsatisfactory chemical stability limit their use as electrocatalysts.[14,15] As interactions between different metal ions can in principle lead to well-tuneable electronic properties, fabrication of mixed-metal coordination complexes, particularly the ones based on metal clusters, represents an effective strategy to boost the performance of electrocatalysts.[16–20] For example, Bu *et al.* synthesized hierarchical bimetal–organic nanostructures with trinuclear units (Co and Ni) showing excellent OER catalytic

activity and high stability.[19] Zhang and co-workers prepared a bimetallic metal–organic framework (MOF) by modifying an Fe$_3$ cluster with a Co$_2$ unit that exhibited exceptional electrocatalytic performance toward the OER.[20]

Calixarene-based coordination clusters have been extensively developed because of their interesting structures[21–28] and wide application in many fields, such as gas adsorption and separation,[29–33] catalysis,[34–41] and drug delivery.[42,43] Recently, we have been interested in the synthesis of diverse thiacalixarene-supported coordination complexes possessing polynuclear secondary building units (PSBUs) and in the exploration of the correlation between their structural features and photocatalytic or electrocatalytic applications.[44–50] For instance, the clusters {Co$_{26}$} and {Ni$_{28}$} with high-density possible coordinative unsaturated metal sites were synthesized from (Co/Ni)$_4$-thiacalixarene PSBUs and showed a high OER performance.[48] Very recently, we reported a bimetallic Co$_4$Mo$_8$ cluster from a Co$_4$-thiacalixarene PSBU capped with an oxothiomolybdate Mo$_8$ unit that can be anchored on nickel foam, achieving an efficient and ultra-stable OER performance due to the Co–Mo synergistic effect.[49]

With these backgrounds in mind, we have synthesized and structurally characterized a series of coordination clusters with the formula {[M$_{16}$(TC4A-SO$_2$)$_4$(H$_2$O)$_4$(BTTAB)$_8$] (+solvents)}, including two monometallic clusters **Co$_{16}$** and **Fe$_{16}$**, and three bimetallic clusters **{CoFe}$_{16}$-a**, **{CoFe}$_{16}$-b** and **{CoFe}$_{16}$-c**, which were built from four M$_4$-(TC4A-SO$_2$) PSBUs and eight BTTAB ligands (M = Co and/or Fe; H$_4$TC4A-SO$_2$ = *p-tert*-butyl-sulfonylcalix[4]arene; H$_2$BTTAB = 1,3-bis(2*H*-tetrazol-5-yl) benzene, Scheme S1†). Interestingly, the bimetallic cluster

[a]School of Chemistry and Chemical Engineering, Institute for Innovative Materials and Energy, Yangzhou University, Yangzhou, Jiangsu 225002, P. R. China
[b]School of Petrochemical Engineering, Liaoning Petrochemical University, Fushun, Liaoning 113001, P. R. China. E-mail: biyanfeng@lnpu.edu.cn

{CoFe}$_{16}$-**b** exhibited a better electrocatalytic OER performance compared with other bimetallic clusters ({CoFe}$_{16}$-**a** and {CoFe}$_{16}$-**c**) with different Co : Fe ratios as well as the monometallic clusters (**Co**$_{16}$ and **Fe**$_{16}$), showing obvious Co–Fe ratio-dependent synergistic effects on the OER.

Experimental section

Materials and measurements

p-tert-Butylsulfonylcalix[4]arene (H$_4$TC4A-SO$_2$) and 1,3-bis(2*H*-tetrazol-5-yl)benzene (BTTAB) were synthesized according to the literature method,[51–53] and other reagents were from commercial sources and used without further purification. Powder X-ray diffraction (PXRD) measurements were performed on a Bruker D8 VENTURE diffractometer with Cu-Kα radiation. Fourier transform infrared (FT-IR) spectra (KBr pellets) were obtained using a PerkinElmer Spectrum GX spectrometer. Thermal gravimetric analysis (TGA) was performed on a TA Q600 thermogravimetric analyzer. X-ray photoelectron spectroscopy (XPS) measurements were performed with an ESCALAB 250Xi using a monochromatic Al Kα X-ray source (1486.6 eV). The morphology of the electrode was observed using a scanning electron microscope (SEM, Hitachi, S-4800). The composition of the samples was characterized by energy-dispersive X-ray spectroscopy (EDX) coupled with SEM. Inductively coupled plasma atomic emission spectroscopy (ICP-AES, Elan DRC-e Plasma mass spectrometer) was performed to investigate the molar ratio of Co and Fe in the mixed-metal clusters. The electrochemical measurements were performed on a CHI660e (Chenhua, Shanghai) electrochemical workstation.

Preparation of the coordination clusters

Synthesis of {[Co$_{16}$(TC4A-SO$_2$)$_4$(H$_2$O)$_4$(BTTAB)$_8$] (+solvents)} (Co$_{16}$). Light red block crystals of cluster **Co**$_{16}$ were synthesized and crystallized from the solvothermal reaction of a mixture of H$_4$TC4A-SO$_2$ (0.072 g, 0.10 mmol), CoCl$_2$·6H$_2$O (0.1 g, 0.40 mmol), BTTAB (0.0214 g, 0.20 mmol), ethanol (CH$_3$CH$_2$OH, 5 mL), and *N,N′*-dimethylformamide (DMF, 5 mL), which was stirred under ambient conditions for 10 min and transferred to a 20 mL Teflon-lined autoclave. The mixture was maintained at 140 °C for 3 days and then slowly cooled to 20 °C at about 4 °C h^{-1}. The crystals were isolated by filtration, washed with CH$_3$CH$_2$OH/DMF (v : v = 1 : 1), and dried in air. Yield: *ca.* 70% based on H$_4$TC4A-SO$_2$.

Synthesis of {[Fe$_{16}$(TC4A-SO$_2$)$_4$(H$_2$O)$_4$(BTTAB)$_8$] (+solvents)} (Fe$_{16}$). Brown block crystals of **Fe**$_{16}$ were obtained under the same reaction conditions as those of **Co**$_{16}$, except for that FeCl$_3$·6H$_2$O (0.08 g, 0.40 mmol) was used in place of CoCl$_2$·6H$_2$O (0.1 g, 0.40 mmol). Yield: *ca.* 65% based on H$_4$TC4A-SO$_2$.

Synthesis of {[(CoFe)$_{16}$(TC4A-SO$_2$)$_4$(H$_2$O)$_4$(BTTAB)$_8$] (+solvents)}

Synthesis of {CoFe}$_{16}$-a. Light red block crystals were synthesized under the same reaction conditions as those of **Co**$_{16}$, except for that CoCl$_2$·6H$_2$O (0.075 g, 0.30 mmol) and FeCl$_3$·6H$_2$O (0.02 g, 0.10 mmol) were used in place of CoCl$_2$·6H$_2$O (0.1 g, 0.40 mmol). Yield: *ca.* 55% based on H$_4$TC4A-SO$_2$. The molar ratio of Co and Fe was 24.10 : 1 based on ICP analysis.

Synthesis of {CoFe}$_{16}$-b. Dark red block crystals were synthesized under the same reaction conditions as those of **Co**$_{16}$, except for that CoCl$_2$·6H$_2$O (0.05 g, 0.20 mmol) and FeCl$_3$·6H$_2$O (0.04 g, 0.20 mmol) were used in place of CoCl$_2$·6H$_2$O (0.1 g, 0.40 mmol). Yield: *ca.* 60% based on H$_4$TC4A-SO$_2$. The molar ratio of Co and Fe was 1.54 : 1 based on ICP analysis.

Synthesis of {CoFe}$_{16}$-c. Dark red block crystals were synthesized under the same reaction conditions as those of **Co**$_{16}$, except for that CoCl$_2$·6H$_2$O (0.025 g, 0.10 mmol) and FeCl$_3$·6H$_2$O (0.06 g, 0.30 mmol) were used in place of CoCl$_2$·6H$_2$O (0.1 g, 0.40 mmol). Yield: *ca.* 55% based on H$_4$TC4A-SO$_2$. The molar ratio of Co and Fe was 1 : 1.42 based on ICP analysis.

Note: there are a large number of solvent molecules in the crystal lattice that could be released under ambient conditions and thus reliable results for the elemental analysis of clusters could not be obtained.

X-ray crystallography

The intensity data were recorded on a Bruker D8 QUEST with Mo-Kα (λ = 0.71073 Å). The crystal structures were solved using direct methods and refined by employing full-matrix least squares on F^2 (SHELXTL-2014).[54] All non-hydrogen atoms were refined anisotropically except for solvent molecules, and hydrogen atoms of the organic ligands were generated theoretically onto the specific atoms and refined isotropically with fixed thermal factors. The diffraction data were treated by the "SQUEEZE" method as implemented in PLATON,[55] which significantly improved the crystal data. Details of the structure solution for the three clusters **Co**$_{16}$, **Fe**$_{16}$, and {CoFe}$_{16}$-**b** (as an example) are given in Table S1.† CCDC numbers 2153012 (**Co**$_{16}$), 2153013 (**Fe**$_{16}$), and 2153014 ({CoFe}$_{16}$-**b**)† contain the supplementary crystallographic data for this paper, which are available free from the Cambridge Crystallography Data Centre (CCDC).

Preparation of the working electrode

10 mg of activated samples (crystals dried in a vacuum at 80 °C for 10 h) was dissolved in 2 mL of chloroform by ultrasonication to form a homogeneous solution, and then various contents of the above suspension were dropped on both sides of the carbon paper (CP, 0.5 × 2 cm^2, treated with concentrated nitric acid, ethanol, and water successively before use). Subsequently, the CP covered with a catalyst was dried in a vacuum at 80 °C for 10 h and used as the working electrode (denoted as **Co**$_{16}$/CP, {CoFe}$_{16}$-**a**/CP, {CoFe}$_{16}$-**b**/CP, {CoFe}$_{16}$-**c**/CP and **Fe**$_{16}$/CP, respectively).

Electrochemical measurements

The electrochemical measurements were performed with an electrochemical workstation in a standard three-electrode

This journal is © the Partner Organisations 2023

Inorg. Chem. Front., 2023, **10**, 926–933 | **927**

system setup with Hg/HgO (saturated KCl) as the reference electrode, a carbon rod (6 mm) as the counter electrode, and the catalyst-modified CP as the working electrode. Linear sweep voltammetry (LSV) was recorded in N_2-saturated 1.0 M KOH at a scan rate of 5 mV s^{-1} to obtain the polarization curves. The potentials were referenced to a reversible hydrogen electrode (RHE) according to the Nernst equation: $E_{RHE} = E_{Hg/HgO} + 0.098 + 0.0592 \times 14$. The overpotential ($\eta$) was calculated according to the following formula: $\eta = E_{RHE} - 1.23$ V, and the current density was normalized to the effective geometrical surface area. To estimate the electrochemical active surface area (ECSA) of the catalyst, CV was used to measure the double-layer capacitance (C_{dl}) under the potential window of 1.027–1.127 V $vs.$ RHE at various scan rates of 10–60 mV s^{-1}.[11,49] Electrochemical impedance spectroscopy (EIS) measurements were carried out at 1.53 V $vs.$ RHE over the frequency range of 0.01 Hz to 100 kHz. A 5 mV amplitude of sinusoidal potential perturbation was used in the measurements. All electrodes were subjected to an activation process until there was no change between the two LSV tests.

Chronoamperometry was performed at the overpotential corresponding to the current density of 10 mA cm^{-2}.

Results and discussion

Structures and characterization

Single-crystal X-ray diffraction revealed that the **Co$_{16}$** crystals crystallize in the tetragonal system with the space group $I4/m$. In **Co$_{16}$**, there are three crystallographically independent Co centres (Co1, Co2, and Co3) and each is six-coordinated by one axial sulfonyl oxygen atom, two phenoxo μ_2-O atoms, one μ_4-O atom from a water molecule, and two terminal nitrogen atoms from two different BTTAB ligands, resulting in an octahedral

coordination environment. Four adjacent Co sites (Co1, Co2, Co3, and Co2A) are shielded by a cone-shaped TC4A-SO$_2$ ligand to form a shuttlecock-like Co$_4$-(TC4A-SO$_2$) PSBU with weakly coordinated μ_4-OH$_2$ at the bottom (Fig. S1†). As shown in Fig. 1a, four Co$_4$-(TC4A-SO$_2$) SBUs in a square arrangement are bridged by eight BTTAB ligands forming a box-like entity. In **Co$_{16}$**, each PSBU is bonded by four BTTAB ligands (Fig. S2a†) and each BTTAB links two SBUs through four terminal nitrogen atoms (Fig. S2b†).

Co$_{16}$ is similar to the window frame-like {Co$_{16}$} square reported except for the following minor differences.[56] The reported {Co$_{16}$} square crystallizes in the monoclinic system with the space group Cc. The coordination modes of the PSBUs and BTTAB ligands are affected by the use of different solvents (Fig. S3†). It is worth noting that the different coordination geometries of the BTTAB ligand lead to the different stacking modes of the clusters. Notably, the connection of Co$_4$-TC4A (H$_4$TC4A = p-tert-butylthiacalix[4]arene) units and the BTTAB ligands gives rise to different types of architectures. For example, a tetrahedral prismatic {Co$_{32}$} coordination cage was constructed by the assembly of Co$_4$-TC4A PSBUs and in $situ$-generated BTTAB ligands.[57] In addition, a 1D coordination polymer was built from the linkage of Co$_4$-TC4A PSBUs and BTTAB ligands.[58] These observations demonstrate that the various coordination geometries of BTTAB facilitate the fabrication of different architectures.

Fe$_{16}$ crystallizes in a low symmetry system (monoclinic $C2/c$) and features a similar box-like framework to that of **Co$_{16}$** (Fig. 1c). There are eight crystallographically independent Fe centres (Fe1–Fe8) each of which shows a similar coordinated atom species to that in **Co$_{16}$** (Fig. S4a†). However, the different bridging modes of BTTAB ligands with Fe$_4$-(TC4A-SO$_2$) PSBUs are responsible for the different crystallization properties. In **Co$_{16}$**, two crystallographically symmetric BTTAB ligands
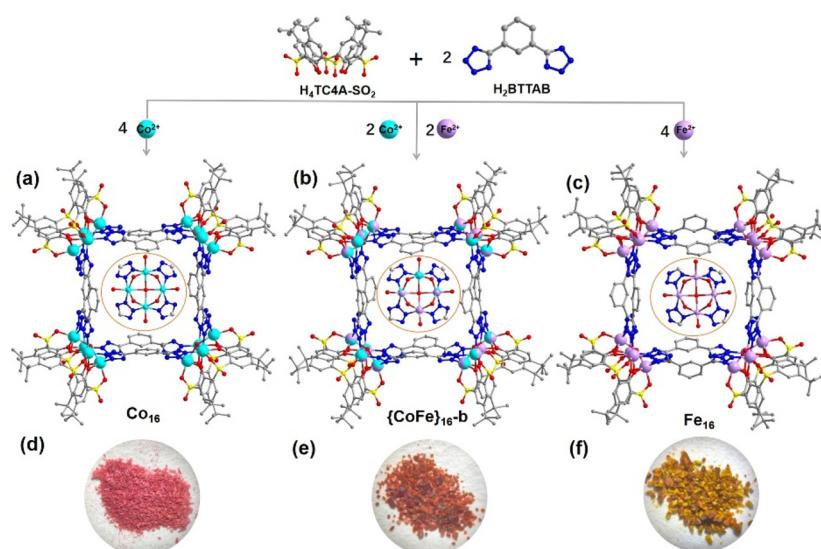
Fig. 1 Schematic illustration of the syntheses of **Co$_{16}$**, {CoFe}$_{16}$-**b** and **Fe$_{16}$**: (a–c) the crystal structures and the coordination mode of metal ions (inset) and (d–f) the photograph of the crystals. Hydrogen atoms are omitted for clarity.

connect with two adjacent tetranuclear PSBUs in an opposite mode (Fig. S2b†). However, two asymmetric BTTAB ligands are arranged in the same direction in Fe_{16} (Fig. S4b†). The more detailed structure description without considering disorders shows that all the BTTAB ligands bond with the PSBUs by two pairs of terminal nitrogen atoms in Co_{16} (Fig. 1a and S2b†). By comparison, one BTTAB ligand between two Fe_4 PSBUs displays the same bridging mode as that in Co_{16} while the other one coordinates to two PSBUs by one terminal nitrogen atom and one side nitrogen atom from the two tetrazole units simultaneously (Fig. 1c and S3†). The discrete clusters of Co_{16} are stacked through molecular interactions into an extended supramolecular structure with square cells (Fig. S5a†) while the square cells are occupied by the BTTAB ligands in Fe_{16} (Fig. S5b†).

$\{CoFe\}_{16}$-**b** is selected to represent the mixed metal analogues and is structurally characterized by single crystal X-ray diffraction (Fig. 1b). $\{CoFe\}_{16}$-**b** is almost identical to Co_{16} except for that parts of Co sites in the Co_4-(TC4A-SO$_2$) PSBU are substituted by Fe sites. The ratio of Co and Fe determined by X-ray crystallography is $3:2$ (molar ratio) for $\{CoFe\}_{16}$-**b**, which is close to the value of $1.54:1$ confirmed by the ICP experiment (Fig. 1b). $\{CoFe\}_{16}$-**a** and $\{CoFe\}_{16}$-**c** are identified by PXRD, FT-IR, and unit-cell comparison with Co_{16} (Fig. S6–S8†).

The PXRD patterns demonstrate that the as-synthesized Co_{16}, $\{CoFe\}_{16}$-**a**, $\{CoFe\}_{16}$-**b**, and $\{CoFe\}_{16}$-**c** possess the same characteristic diffraction peak positions confirming the isostructural coordination clusters (Fig. S6†). The phase purity of Fe_{16} with low symmetry is also confirmed by PXRD (Fig. S7†). The FT-IR spectra show the characteristic vibrations of TC4A-SO$_2$ and BTTAB in these clusters (Fig. S8†). TGA experiments were performed to check the thermal stability of the coordination clusters Co_{16}, $\{CoFe\}_{16}$-**b**, and Fe_{16} (for details see Fig. S9–S11†). ICP-AES elemental analysis showed that the molar ratios of Co and Fe in $\{CoFe\}_{16}$-**a**, $\{CoFe\}_{16}$-**b**, and $\{CoFe\}_{16}$-**c** are $24.10:1$, $1.54:1$, and $1:1.42$, respectively (Table S3†). We failed to obtain the bimetallic coordination clusters with the metal molar ratio corresponding to the initial feeding materials $CoCl_2 \cdot 6H_2O$ and $FeCl_3 \cdot 6H_2O$. These observations demonstrated that there is coordination competition between Co and Fe with the TC4A-SO$_2$ ligand, and Co ions are more prone to coordination under the same conditions. Additionally, the charge balance consideration, BVS calculations (Table S2†), and XPS measurements indicate that all metal ions are divalent. We optimized the synthetic conditions and tried to definitively establish the source of the reductant for Fe^{3+} during the synthesis to produce the Fe^{2+} sites. When CH_3CH_2OH and/or DMF were substituted or omitted, the title clusters could not be achieved. In addition, when iron(II) chloride was directly used, only amorphous precipitates were formed. However, we can obtain pure crystals by simple filtration and washing when iron(III) chloride is used. We speculated that the reduction of the Fe(III) ion to the Fe(II) ion in the synthesis might facilitate the efficient preparation of ion clusters, which is consistent with the fact that thiacalixarenes readily form divalent complexes with transition metals as reported in the literature.[24,50,59–61]

Electrochemical properties

The active Co_{16}, $\{CoFe\}_{16}$-**a**, $\{CoFe\}_{16}$-**b**, $\{CoFe\}_{16}$-**c** and Fe_{16} materials are impregnated in chloroform solution and directly deposited on carbon paper (Co_{16}/CP, $\{CoFe\}_{16}$-**a**/CP, $\{CoFe\}_{16}$-**b**/CP, $\{CoFe\}_{16}$-**c**/CP and Fe_{16}/CP) for the OER. The OER performance of Co_{16}/CP, $\{CoFe\}_{16}$-**a**/CP, $\{CoFe\}_{16}$-**b**/CP, $\{CoFe\}_{16}$-**c**/CP and Fe_{16}/CP was evaluated with a standard three-electrode system in N_2-saturated 1 M KOH solution at room temperature. All the potentials were calibrated against the reversible hydrogen electrode (RHE) for comparison. Preliminary investigations demonstrated that $\{CoFe\}_{16}$-**b**/CP exhibited better electrochemical performance. Thus, the experimental conditions were determined by $\{CoFe\}_{16}$-**b**/CP. Based on the linear sweep voltammetry (LSV) curve, the optimal loading of $\{CoFe\}_{16}$-**b**/CP is 1.5 mg cm^{-2} (Fig. S12†). Fig. 2a shows the polarization curves of Co_{16}/CP, $\{CoFe\}_{16}$-**a**/CP, $\{CoFe\}_{16}$-**b**/CP, $\{CoFe\}_{16}$-**c**/CP and Fe_{16}/CP. Compared with pure CP, the Co_{16}/CP, $\{CoFe\}_{16}$-**a**/CP, $\{CoFe\}_{16}$-**b**/CP, $\{CoFe\}_{16}$-**c**/CP, and Fe_{16}/CP catalysts show significantly enhanced electrocatalytic activity for the OER. Impressively, $\{CoFe\}_{16}$-**b**/CP exhibits superior OER performance with an overpotential of 285.3 mV at $|j| = 10$ mA cm^{-2}, which is distinctly better than those of Co_{16}/CP (369.8 mV), $\{CoFe\}_{16}$-**a**/CP (298.8 mV), $\{CoFe\}_{16}$-**c**/CP (290.8 mV), and Fe_{16}/CP (350.8 mV). The OER performance of the different catalysts was further determined in terms of their Tafel slopes (Fig. 2b). The $\{CoFe\}_{16}$-**b**/CP catalyst has a Tafel slope of 72.8 mV dec^{-1}, which is lower than those of Co_{16}/CP (92.6 mV dec^{-1}), $\{CoFe\}_{16}$-**a**/CP (87.5 mV dec^{-1}), $\{CoFe\}_{16}$-**c**/CP (75.1 mV dec^{-1}), and Fe_{16}/CP (89.1 mV dec^{-1}), suggesting that better kinetics is involved which facilitates the OER electrocatalytic activity. Electrochemical impedance spectroscopy (EIS) was used to investigate the charge transfer behaviour of the OER process (Fig. 2c). The Nyquist plots and the corresponding equivalent circuit model reveal that the charge transfer resistance (R_{ct}) of $\{CoFe\}_{16}$-**b**/CP (3.7 Ω) is smaller than those of Co_{16}/CP (10.0 Ω), $\{CoFe\}_{16}$-**a**/CP (5.4 Ω), $\{CoFe\}_{16}$-**c**/CP (5.2 Ω), and Fe_{16}/CP (9.1 Ω), indicating that $\{CoFe\}_{16}$-**b**/CP exhibits a faster charge transfer rate.

To gain more insights into the catalytic activity of the catalysts, the electrochemical active surface area (ECSA)[11] was determined for the Co_{16}/CP, $\{CoFe\}_{16}$-**a**/CP, $\{CoFe\}_{16}$-**b**/CP, $\{CoFe\}_{16}$-**c**/CP and Fe_{16}/CP catalysts (Fig. S13a–e†) via calculating the electrochemical double-layer capacitance (C_{dl}). Upon plotting $\Delta J/2 = (J_a - J_c)/2$ at 1.07 V vs. RHE against the scan rate (Fig. 2d), $\{CoFe\}_{16}$-**b**/CP shows a higher C_{dl} (6.61 mF cm^{-2}) compared with those of Co_{16}/CP (2.18 mF cm^{-2}), $\{CoFe\}_{16}$-**a**/CP (3.08 mF cm^{-2}), $\{CoFe\}_{16}$-**c**/CP (4.98 mF cm^{-2}), and Fe_{16}/CP (2.60 mF cm^{-2}), indicating that $\{CoFe\}_{16}$-**b**/CP possesses a larger ECSA at the solid–liquid interface. These results confirm that the synergistic effect between Co and Fe with an optimized molar ratio in the $\{CoFe\}_{16}$-**b** cluster can lead to improved kinetics, a larger ECSA, and a faster charge transfer rate, thus boosting the OER activity. The stability of the pre-

This journal is © the Partner Organisations 2023

Inorg. Chem. Front., 2023, **10**, 926–933 | **929**
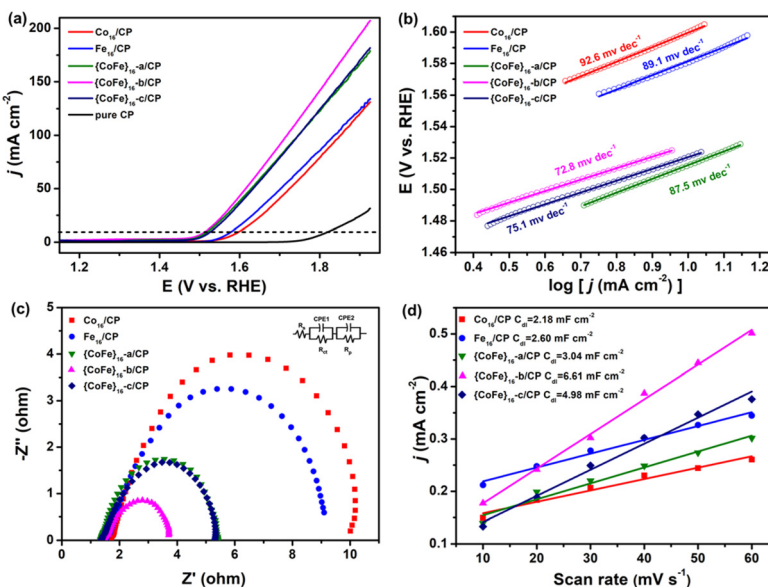
Fig. 2 (a) OER polarization curves and (b) Tafel plots for the different electrocatalysts in 1 M KOH solution. (c) Nyquist plots for different electrocatalysts recorded at 1.53 V *vs.* RHE (inset: the equivalent circuit model for electrochemical impedance tests). (d) Plots of the charging current density against scan rates of different catalysts for determining the ECSA.

pared catalysts was initially investigated using the current–time (i–t) method. The i–t curve recorded at 1.60 V *vs.* RHE, shown in Fig. S13f†, suggests the excellent stability of {**CoFe**}$_{16}$-**b**/CP as a negligible shift in the current density of 10 mA cm^{-2} was observed after 12 h of continuous OER. It is worthy to note that the OER performance of {**CoFe**}$_{16}$-**b**/CP is comparable to those of other CoFe-based materials, such as FexCoy-P/C nanocomposites,[62] CoFeP and CoFe hydroxide,[63] and FeCo-DACs/NC.[64]

To further investigate the effect of Co and Fe on OER catalysis, XPS measurements for {**CoFe**}$_{16}$-**b** before and after the OER tests were carried out. As shown in Fig. 3a, the Co^{2+} 2p$_{3/2}$ (782.8 eV) peak shifts to a lower binding energy (782.2 eV), while the Fe^{2+} 2p$_{3/2}$ peak shifts to a higher binding energy (from 710.2 eV to 711.1 eV, Fig. 3b). This indicates that a partial electron is transferred from Fe^{2+} to Co^{2+} through, for example, the phenoxo μ$_2$-O atoms. The transition will change the partial density of states of the unfilled metal 3d e$_g$-orbital in bimetal coordination clusters, resulting in an increase in the density of the unoccupied e$_g$ state for Fe and a decrease for Co. It has been demonstrated that the coupling of different metal ions could induce a change of e$_g$ filling and facilitate the OER performance.[16] The main peaks of high-resolution N 1s, O 1s, and S 2p XPS spectra for {**CoFe**}$_{16}$-**b** showed no significant change after the OER (Fig. S14†), indicating that the framework structure of {**CoFe**}$_{16}$-**b** is maintained. The emergence of the new peak at 530.5 eV in high-resolution O 1s is attributed to OH$^-$, which is due to the adsorption between the metal clusters and/or the electrolyte and the weakly coordinated μ$_4$-H$_2$O substituted by OH$^-$ in the base.[49] The peaks at *ca.* 169.5 eV in the high-resolution S 2p XPS spectrum for {**CoFe**}$_{16}$-**b** after catalysis slightly shifted to a lower energy
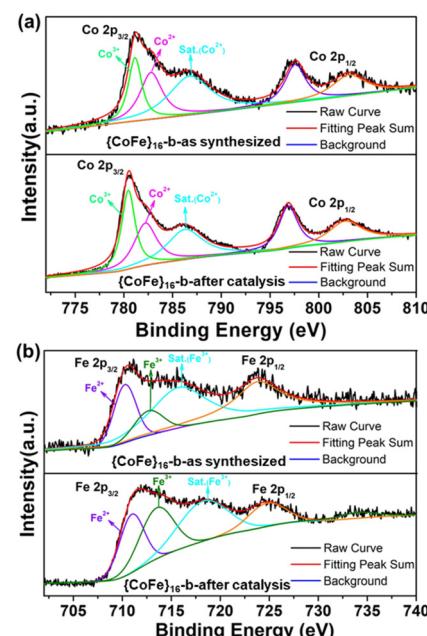

Fig. 3 High-resolution Co 2p (a) and Fe 2p (b) XPS spectra of the as-synthesized {**CoFe**}$_{16}$-**b** and {**CoFe**}$_{16}$-**b** after catalysis (after LSV).

region, which can be assigned to the changes in the coordination environment of –SO$_2$ groups (*e.g.* variation of S–O distances).

The morphologies of the as-prepared electrode and that after the i–t test for {**CoFe**}$_{16}$-**b**/CP were characterized by SEM (Fig. S15†). The uniform distributions of elements Fe, Co, S, O, N, and C were confirmed by elemental mapping analysis. K

was observed after the OER, suggesting the adsorption between the metal cluster and the electrolyte.[49] This observation is consistent with the high-resolution O 1s XPS spectrum (Fig. S14b†) and EDX analysis (Fig. S16†). After the OER, the Fe leak into the resultant filtrate was determined to be 0.76% by ICP-AES analysis. No Co signal is detected in the resultant filtrate. This result further confirms the stability of the {CoFe}$_{16}$-**b** catalyst. The synergistic effect between Co and Fe is established and favourable for improving the OER performance. The catalytic sites might be attributed to the Co/Fe sites by eliminating weakly coordinated H$_2$O (with average M–O distances being 2.188 Å) at the bottom of the M$_4$-(TC4A-SO$_2$) PSBUs by electrolyte substitution.[49]

Conclusions

In summary, a series of thiacalixarene-based coordination clusters **Co$_{16}$**, **{CoFe}$_{16}$-a**, **{CoFe}$_{16}$-b**, **{CoFe}$_{16}$-c**, and **Fe$_{16}$** were synthesized using the solvothermal reaction. The OER performances of these clusters were investigated by experimental means. The catalyst **{CoFe}$_{16}$-b** afforded a lower overpotential and a smaller Tafel slope as compared with bimetallic **{CoFe}$_{16}$-a** and **{CoFe}$_{16}$-c** as well as the pure metal-based **Co$_{16}$** and **Fe$_{16}$**. The excellent electrocatalytic OER performance of **{CoFe}$_{16}$-b** was strongly correlated to the synergistic effect between Co and Fe in PSBUs with an optimized molar ratio, which led to improved kinetics, a larger ECSA, and a faster charge transfer rate. The present work demonstrates that the integration of heterometallic units into cluster-based coordination complexes is a promising strategy to improve their OER electrocatalytic performance.

Author contributions

X.X. Hang and Y.F. Bi conceived and designed the project. X.J. Wang, M.L. Wang, and M.W. Chen performed the experiments and characterization. X.X. Hang and Y.F. Bi analyzed the experimental results and wrote the manuscript with input from the other authors. X.X. Hang and Y.F. Bi provided funding support.

Conflicts of interest

There are no conflicts to declare.

Acknowledgements

References

1 J. D. Blakemore, R. H. Crabtree and G. W. Brudvig, Molecular Catalysts for Water Oxidation, *Chem. Rev.*, 2015, **115**, 12974–13005.

2 H. Y. Jin, C. X. Guo, X. Liu, J. L. Liu, A. Vasileff, Y. Jiao, Y. Zheng and S. Z. Qiao, Emerging Two-Dimensional Nanomaterials for Electrocatalysis, *Chem. Rev.*, 2018, **118**, 6337–6408.

3 T. W. Kim and K. S. Choi, Nanoporous BiVO$_4$ Photoanodes with Dual-Layer Oxygen Evolution Catalysts for Solar Water Splitting, *Science*, 2014, **343**, 990–994.

4 T. Y. Ma, S. Dai, M. Jaroniec and S. Z. Qiao, Metal-Organic Framework Derived Hybrid Co$_3$O$_4$-Carbon Porous Nanowire Arrays as Reversible Oxygen Evolution Electrodes, *J. Am. Chem. Soc.*, 2014, **136**, 13925–13931.

5 H. Over, Surface Chemistry of Ruthenium Dioxide in Heterogeneous Catalysis and Electrocatalysis: From Fundamental to Applied Research, *Chem. Rev.*, 2012, **112**, 3356–3426.

6 L. C. Seitz, C. F. Dickens, K. Nishio, Y. Hikita, J. Montoya, A. Doyle, C. Kirk, A. Vojvodic, H. Y. Hwang, J. K. Norskov and T. F. Jaramillo, A Highly Active and Stable IrO$_x$/SrIrO$_3$ Catalyst for the Oxygen Evolution Reaction, *Science*, 2016, **353**, 1011–1014.

7 B. M. Hunter, H. B. Gray and A. M. Müller, Earth-Abundant Heterogeneous Water Oxidation Catalysts, *Chem. Rev.*, 2016, **116**, 14120–14136.

8 I. Roger, M. A. Shipman and M. D. Symes, Earth-Abundant Catalysts for Electrochemical and Photoelectrochemical Water Splitting, *Nat. Rev. Chem.*, 2017, **1**, 0003.

9 J. Du, F. Li and L. C. Sun, Metal-Organic Frameworks and Their Derivatives as Electrocatalysts for the Oxygen Evolution Reaction, *Chem. Soc. Rev.*, 2021, **50**, 2663–2695.

10 L. J. Kong, M. Zhong, W. Shuang, Y. H. Xu and X. H. Bu, Electrochemically Active Sites inside Crystalline Porous Materials for Energy Storage and Conversion, *Chem. Soc. Rev.*, 2020, **49**, 2378–2407.

11 X. L. Wang, L. Z. Dong, M. Qiao, Y. J. Tang, J. Liu, Y. F. Li, S. L. Li, J. X. Su and Y. Q. Lan, Exploring the Performance Improvement of the Oxygen Evolution Reaction in a Stable Bimetal-Organic Framework System, *Angew. Chem., Int. Ed.*, 2018, **57**, 9660–9664.

12 F. L. Li, Q. Shao, X. Q. Huang and J. P. Lang, Nanoscale Trimetallic Metal-Organic Frameworks Enable Efficient Oxygen Evolution Electrocatalysis, *Angew. Chem., Int. Ed.*, 2018, **57**, 1888–1892.

13 Q. N. Liang, J. M. Chen, F. L. Wang and Y. W. Li, Transition Metal-Based Metal-Organic Frameworks for Oxygen Evolution Reaction, *Coord. Chem. Rev.*, 2020, **424**, 213488.

14 P. Q. Liao, J. Q. Shen and J. P. Zhang, Metal-Organic Frameworks for Electrocatalysis, *Coord. Chem. Rev.*, 2018, **373**, 22–48.

15 I. Stassen, N. Burtch, A. Talin, P. Falcaro, M. Allendorf and R. Ameloot, An Updated Roadmap for the Integration of

This journal is © the Partner Organisations 2023

Inorg. Chem. Front., 2023, **10**, 926–933 | **931**

Metal-Organic Frameworks with Electronic Devices and Chemical Sensors, *Chem. Soc. Rev.*, 2017, **46**, 3185–3241.

16 S. L. Zhao, Y. Wang, J. C. Dong, C. T. He, H. J. Yin, P. F. An, K. Zhao, X. F. Zhang, C. Gao, L. J. Zhang, J. W. Lv, J. X. Wang, J. Q. Zhang, A. M. Khattak, N. A. Khan, Z. X. Wei, J. Zhang, S. Q. Liu, H. J. Zhao and Z. Y. Tang, Ultrathin Metal-Organic Framework Nanosheets for Electrocatalytic Oxygen Evolution, *Nat. Energy*, 2016, **1**, 16184–16913.

17 Y. T. Xu, Z. M. Ye, J. W. Ye, L. M. Cao, R. K. Huang, J. X. Wu, D. D. Zhou, X. F. Zhang, C. T. He, J. P. Zhang and X. M. Chen, Non-3d Metal Modulation of a Cobalt Imidazolate Framework for Excellent Electrocatalytic Oxygen Evolution in Neutral Media, *Angew. Chem., Int. Ed.*, 2019, **58**, 139–143.

18 W. R. Cheng, X. Zhao, H. Su, F. M. Tang, W. Che, H. Zhang and Q. H. Liu, Lattice-Strained Metal-Organic-Framework Arrays for Bifunctional Oxygen Electrocatalysis, *Nat. Energy*, 2019, **4**, 115–122.

19 W. Zhou, D. D. Huang, Y. P. Wu, J. Zhao, T. Wu, J. Zhang, D. S. Li, C. H. Sun, P. Y. Feng and X. H. Bu, Stable Hierarchical Bimetallic-Organic Nanostructures as High-Performance Electrocatalysts for the Oxygen Evolution Reaction, *Angew. Chem., Int. Ed.*, 2019, **58**, 4227–4231.

20 J. Q. Shen, P. Q. Liao, D. D. Zhou, C. T. He, J. X. Wu, W. X. Zhang, J. P. Zhang and X. M. Chen, Modular and Stepwise Synthesis of a Hybrid Metal-Organic Framework for Efficient Electrocatalytic Oxygen Evolution, *J. Am. Chem. Soc.*, 2017, **139**, 1778–1781.

21 X. Q. Hu, J. Chai, C. Zhang, J. X. Lang, S. P. Kelley, S. S. Feng, B. Liu, D. A. Atwood and J. L. Atwood, Biomimetic Self-Assembly of Co^{II}-Seamed Hexameric Metal–Organic Nanocapsules, *J. Am. Chem. Soc.*, 2019, **141**, 9151–9154.

22 K. Z. Su, M. Y. Wu, D. Q. Yuan and M. C. Hong, Interconvertible Vanadium-Seamed Hexameric Pyrogallol [4]arene Nanocapsules, *Nat. Commun.*, 2018, **9**, 4941.

23 R. Kumar, Y. O. Lee, V. Bhalla, M. Kumar and J. S. Kim, Recent Developments of Thiacalixarene Based Molecular Motifs, *Chem. Soc. Rev.*, 2014, **43**, 4824–4870.

24 Y. F. Bi, S. C. Du and W. P. Liao, Thiacalixarene–Based Nanoscale Polyhedral Coordination Cages, *Coord. Chem. Rev.*, 2014, **276**, 61–72.

25 M. Liu, W. P. Liao, C. H. Hu, S. C. Du and H. J. Zhang, Calixarene-Based Nanoscale Coordination Cages, *Angew. Chem., Int. Ed.*, 2012, **51**, 1585–1588.

26 F. R. Dai and Z. Q. Wang, Modular Assembly of Metal–Organic Supercontainers Incorporating Sulfonylcalixarenes, *J. Am. Chem. Soc.*, 2012, **134**, 8002–8005.

27 K. C. Xiong, F. L. Jiang, Y. L. Gai, D. Q. Yuan, L. Chen, M. Y. Wu, K. Z. Su and M. C. Hong, Truncated Octahedral Coordination Cage Incorporating Six Tetranuclear-Metal Building Blocks and Twelve Linear Edges, *Chem. Sci.*, 2012, **3**, 2321–2325.

28 H. T. Han, L. Kan, P. Li, G. S. Zhang, K. Y. Li, W. P. Liao, Y. L. Liu, W. Chen and C. H. Hu, 4.8 nm Concave {M$_{72}$} (M=Co, Ni, Fe) Metal-Organic Polyhedral Capped by 18 Calixarenes, *Sci. China: Chem.*, 2021, **64**, 426–431.

29 F. R. Dai, U. Sambasivam, A. J. Hammerstrom and Z. Q. Wang, Synthetic Supercontainers Exhibit Distinct Solution versus Solid State Guest-Binding Behavior, *J. Am. Chem. Soc.*, 2014, **136**, 7480–7491.

30 X. X. Hang, B. Liu, X. F. Zhu, S. T. Wang, H. T. Han, W. P. Liao, Y. L. Liu and C. H. Hu, Discrete {Ni$_{40}$} Coordination Cage: A Calixarene-Based Johnson-Type (J_{17}) Hexadecahedron, *J. Am. Chem. Soc.*, 2016, **138**, 2969–2972.

31 X. X. Hang, B. Liu, S. T. Wang, Y. L. Liu and W. P. Liao, A Metal-Calixarene Coordination Coordination Nanotube with 5-(pyrimidine-5-yl)Isophthalic Acid, *Dalton Trans.*, 2018, **47**, 1782–1785.

32 D. T. Geng, M. Zhang, X. X. Hang, W. J. Xie, Y. C. Qin, Q. Li, Y. F. Bi and Z. P. Zheng, A 2D Metal-Thiacalix[4]arene Porous Coordination Polymer with 1D Channels: Gas Absorption/Separation and Frequency Response, *Dalton Trans.*, 2018, **47**, 9008–9013.

33 D. T. Geng, X. Han, Y. F. Bi, Y. C. Qin, Q. Li, L. L. Huang, K. Zhou, L. J. Song and Z. P. Zheng, Merohedral Icosahedral M$_{48}$ (M = Co^{II}, Ni^{II}) Cage Clusters Supported by Thiacalix[4]arene, *Chem. Sci.*, 2018, **9**, 8535–8541.

34 N. Bhuvaneswari, K. P. Annamalai, F. R. Dai and Z. N. Chen, Pyridinium Functionalized Coordination Containers as Highly Efficient Electrocatalysts for Sustainable Oxygen Evolution, *J. Mater. Chem. A*, 2017, **5**, 23559–23565.

35 K. Y. Li, Z. H. Zhuang, W. Chen and W. P. Liao, Anion-Directed Assembly of Nickel-Calixarene Complexes: Constructing Isolated {Ni$_8$}, {Ni$_{20}$}, {Ni$_{24}$}, and {Ni$_{32}$} Clusters, *Cryst. Growth Des.*, 2020, **20**, 4164–4168.

36 Y. P. Qiao, L. Zhang, J. Li, W. Lin and Z. Q. Wang, Switching on Supramolecular Catalysis via Cavity Mediation and Electrostatic Regulation, *Angew. Chem., Int. Ed.*, 2016, **55**, 12778–12782.

37 C. X. Tan, J. J. Jiao, Z. J. Li, Y. Liu, X. Han and Y. Cui, Design and Assembly of a Chiral Metallosalen-Based Octahedral Coordination Cage for Supramolecular Asymmetric Catalysis, *Angew. Chem., Int. Ed.*, 2018, **57**, 2085–2090.

38 S. T. Wang, X. H. Gao, X. X. Hang, X. F. Zhu, H. T. Han, W. P. Liao and W. Chen, Ultrafine Pt Nanoclusters Confined in a Calixarene-Based {Ni$_{24}$} Coordination Cage for High-Efficient Hydrogen Evolution Reaction, *J. Am. Chem. Soc.*, 2016, **138**, 16236–16239.

39 S. T. Wang, X. H. Gao, X. X. Hang, X. F. Zhu, H. T. Han, X. K. Li, W. P. Liao and W. Chen, Calixarene-Based {Ni$_{18}$} Coordination Wheel: Highly Efficient Electrocatalyst for the Glucose Oxidation and Template for the Homogenous Cluster Fabrication, *J. Am. Chem. Soc.*, 2018, **140**, 6271–6277.

40 Y. Fang, J. L. Li, T. Togo, F. Y. Jin, Z. F. Xiao, L. J. Liu, H. Drake, X. Z. Lian and H. C. Zhou, Ultra-Small Face-Centered-Cubic Ru Nanoparticles Confined within a

932 | *Inorg. Chem. Front.*, 2023, **10**, 926–933

This journal is © the Partner Organisations 2023

Porous Coordination Cage for Dehydrogenation, *Chem*, 2018, **4**, 555–563.

41 Y. Fang, Z. F. Xiao, J. L. Li, C. Lollar, L. J. Liu, X. Z. Lian, S. Yuan, X. Banerjee, P. Zhang and H. C. Zhou, Formation of a Highly Reactive Cobalt Nanocluster Crystal within a Highly Negatively Charged Porous Coordination Cage, *Angew. Chem., Int. Ed.*, 2018, **57**, 5283–5287.

42 S. C. Du, T. Q. Yu, W. P. Liao and C. H. Hu, Structure Modeling, Synthesis and X-ray Diffraction Determination of an Extra-Large Calixarene-Based Coordination Cage and Its Application in Drug Delivery, *Dalton Trans.*, 2015, **44**, 14394–14402.

43 C. He, X. Z. Chen, C. Z. Sun, L. Y. Zhang, W. F. Xu, S. Y. Zhang, Z. Q. Wang and F. R. Dai, Decahexanuclear Zinc(II) Coordination Container Featuring a Flexible Tetracarboxylate Ligand: A Self-Assembly Supermolecule for Highly Efficient Drug Delivery of Anti-Inflammatory Agents, *ACS Appl. Mater. Interfaces*, 2021, **13**, 33812–33820.

44 C. Shi, M. Zhang, X. X. Hang, Y. F. Bi, L. L. Huang, K. Zhou and Z. P. Zheng, Assembly of Thiacalix[4]arene-Supported High-Nuclearity Cd$_{24}$ Cluster with Enhanced Photocatalytic Activity, *Nanoscale*, 2018, **10**, 14448–14454.

45 X. Wang, Y. N. Yu, Z. Wang, J. Zheng, Y. F. Bi and Z. P. Zheng, Thiacalix[4]arene-Protected Titanium-Oxo Clusters: Influence of Ligand Conformation and Ti-S Coordination on the Visible-Light Photocatalytic Hydrogen Production, *Inorg. Chem.*, 2020, **59**, 7150–7157.

46 C. Shi, M. W. Chen, X. Han, Y. F. Bi, L. L. Huang, K. Zhou and Z. P. Zheng, Thiacalix[4]arene-Supported Tetradecanuclear Cobalt Nanocage Cluster as Precursor to Synthesize CoO/Co$_9$S$_8$@CN Composite for Supercapacitor Application, *Inorg. Chem. Front.*, 2018, **5**, 1329–1335.

47 X. X. Hang, W. X. Yang, S. T. Wang, H. T. Han, W. P. Liao and J. B. Jia, Calixarene-Based {Co$_{26}$} Burr Puzzle: An Efficient Oxygen Reduction Catalyst, *ACS Appl. Nano Mater.*, 2019, **2**, 4232–4237.

48 M. W. Chen, M. Zhang, X. Wang, Y. F. Bi, B. K. Chen and Z. P. Zheng, Thiacalixarene-Supported Irregular Co$_{26}$ and Ni$_{28}$ High-Nuclearity Cluster with Pyridyl-Diphosphonates: Strategies to Create Active Metal Sites and Fabricate Multicomponent Materials, *Inorg. Chem.*, 2019, **58**, 6276–6282.

49 M. Zhang, M. W. Chen, Y. F. Bi, L. L. Huang, K. Zhou and Z. P. Zheng, A Bimetallic Co$_4$Mo$_8$ Cluster Built from Mo$_8$ Oxothiomolybdate Capped by a Co$_4$-Thiacalix[4]arene Unit: The Observation of the Co-Mo Synergistic Effect for Binder-Free Electrocatalysts, *J. Mater. Chem. A*, 2019, **7**, 12893–12899.

50 X. X. Hang and Y. F. Bi, Thiacalix[4]arene-Supported Molecular Clusters for Catalytic Applications, *Dalton Trans.*, 2021, **50**, 3749–3758.

51 N. Iki, H. Kumagai, N. Morohashi, K. Ejima, M. Hasegawa, S. Miyanari and S. Miyano, Selective Oxidation of Thiacalix[4]arenes to the Sulfinyl- and Sulfonylcalix[4]arenes and

Their Coordination Ability to Metal Ions, *Tetrahedron Lett.*, 1998, **39**, 7559–7562.

52 N. Morohashi, N. Iki, A. Sugawara and S. Miyano, Selective Oxidation of Thiacalix[4]arenes to the Sulfinyl and Sulfonyl Counterparts and Their Complexation Abilities Toward Metal Ions As Studied by Solvent Extraction, *Tetrahedron*, 2001, **57**, 5557–5563.

53 P. Howlader and P. S. Mukherjee, Face and Edge Directed Self-Assembly of Pd$_{12}$ Tetrahedral Nano-Cages and Their Self-Sorting, *Chem. Sci.*, 2016, **7**, 5893–5899.

54 G. M. Sheldrick, SHELXT-Integrated Space-Group and Crystal Structure Determination, *Acta Crystallogr., Sect. A: Found. Adv.*, 2015, **71**, 3–8.

55 A. L. Spek, PLATON SQUEEZE: A Tool for the Calculation of the Disordered Solvent Contribution to the Calculated Structure Factors, *Acta Crystallogr., Sect. C: Struct. Chem.*, 2015, **71**, 9–18.

56 G. S. Zhang, X. F. Zhu, M. Liu and W. P. Liao, A Window Frame-Like Square Constructed by Bridging Co$_4$-(TC4A-SO$_2$) SBUs with 1,3-bis(2H-tertazol-5-yl)Benzene, *J. Mol. Struct.*, 2018, **1151**, 29–33.

57 Y. F. Bi, S. T. Wang, M. Liu, S. C. Du and W. P. Liao, A Tetragonal Prismatic {Co$_{32}$} Nanocage Based on Thiacalixarene, *Chem. Commun.*, 2013, **49**, 6785–6787.

58 Z. Wang, M. L. Wang, K. He, X. X. Hang and Y. F. Bi, Co$_9$S$_8$@CN Composites Obtained from Thiacalix[4]arene-Based Coordination Polymers for Supercapacitor Applications, *Chem. – Asian J.*, 2021, **16**, 1486–1492.

59 H. Q. Tan, S. C. Du, Y. F. Bi and W. P. Liao, Two Elongated Octahedral Coordination Cages Constructed by M$_4$-TC4A Secondary Building Units (M = Co^{II} and Fe^{II}) and 2,2′-Bipyridine-4,4′-dicarboxylic Acids, *Inorg. Chem.*, 2014, **53**, 7083–7085.

60 H. Q. Tan, S. C. Du, Y. F. Bi and W. P. Liao, Two 2D metal-calixarene aggregates incorporating pre-designed coordination nanocages, *Chem. Commun.*, 2013, **49**, 8211–8213.

61 X. F. Zhu, H. T. Han, X. L. Li, S. T. Wang and W. P. Liao, A calixarene-capped round-cake like {Fe$_{24}$} coordination cage involving the shuttlecock-like Fe$_4$-TC4A SBUs, *Inorg. Chem. Commun.*, 2020, **113**, 107801.

62 W. Hong, M. Kitta and Q. Xu, Bimetallic MOF-Derived FeCo-P/C Nanocomposites as Efficient Catalysts for Oxygen Evolution Reaction, *Small Methods*, 2018, **2**, 1800214.

63 C. Wang, H. Y. Shang, Y. Wang, J. Li, S. Y. Guo, J. Guo and Y. K. Du, A General MOF-Intermediated Synthesis of Hollow CoFe-Based Trimetallic Phosphides Composed of Ultrathin Nanosheets for Boosting Water Oxidation Electrocatalysis, *Nanoscale*, 2021, **13**, 7279–7284.

64 M. Liu, N. Li, S. F. Cao, X. M. Wang, X. Q. Lu, L. J. Kong, Y. H. Xu and X. H. Bu, A "Pre-constrained Metal Twins" Strategy to Prepare Efficient Dual-Metal Atom Catalysts for Cooperative Oxygen Electrocatalysis, *Adv. Mater.*, 2022, **34**, 2107421.

This journal is © the Partner Organisations 2023

Inorg. Chem. Front., 2023, **10**, 926–933 | **933**